THE JOURNAL OF PHYSICAL CHEMISTRY B

Article

pubs.acs.org/JPCB

Electrostatic Control of Polymorphism in Charged Amphiphile Assemblies

Changrui Gao,[†] Honghao Li,[†] Yue Li,[†] Sumit Kewalramani,[†] Liam C. Palmer,[‡] Vinayak P. Dravid,[†] Samuel I. Stupp,[†,‡,§,∥] Monica Olvera de la Cruz,[*,†,‡,⊥,#] and Michael J. Bedzyk[*,†,#]

[†]Department of Materials Science and Engineering, Northwestern University, Evanston, Illinois 60208, United States

[‡]Department of Chemistry, Northwestern University, Evanston, Illinois 60208, United States

[§]Department of Biomedical Engineering, Northwestern University, Evanston, Illinois 60208, United States

[∥]Department of Medicine and Simpson Querrey Institute for BioNanotechnology, Northwestern University, Chicago, Illinois 60611, United States

[⊥]Chemical and Biological Engineering Department, Northwestern University, Evanston, Illinois 60208, United States

[#]Department of Physics and Astronomy, Northwestern University, Evanston, Illinois 60208, United States

Supporting Information

ABSTRACT: Stimuli-induced structural transformations of molecular assemblies in aqueous solutions are integral to nanotechnological applications and biological processes. In particular, pH responsive amphiphiles as well as proteins with various degrees of ionization can reconfigure in response to pH variations. Here, we use in situ small and wide-angle X-ray scattering (SAXS/WAXS), transmission electron microscopy (TEM), and Monte Carlo simulations to show how charge regulation via pH induces morphological changes in the assembly of a positively charged peptide amphiphile (PA). Monte Carlo simulations and pH titration measurements reveal that ionic correlations in the PA assemblies shift the ionizable amine pK ∼ 8 from pK ∼ 10 in the lysine headgroup. SAXS and TEM show that with increasing pH, the assembly undergoes spherical micelle to cylindrical nanofiber to planar bilayer transitions. SAXS/WAXS reveal that the bilayer leaflets are interdigitated with the tilted PA lipid tails crystallized on a rectangular lattice. The details of the molecular packing in the membrane result from interplay between steric and van der Waals interactions. We speculate that this packing motif is a general feature of bilayers comprised of amphiphilic lipids with large ionic headgroups. Overall, our studies correlate the molecular charge and the morphology for a pH-responsive PA system and provide insights into the Å-scale molecular packing in such assemblies.

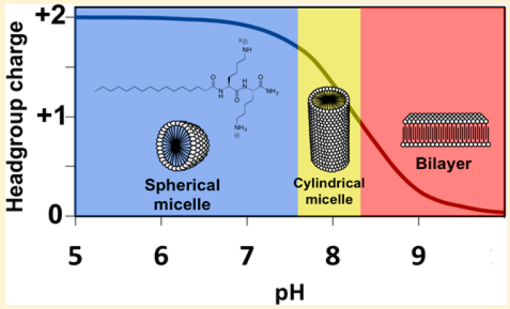

INTRODUCTION

Assemblies of amphiphilic molecules in aqueous solutions and at interfaces are often used as model systems for cell membranes and associated processes and have important nanotechnological applications, including extraction,[1,2] decontamination and remediation,[3] and biosensing.[4] Peptide amphiphiles (PAs), molecules in which a hydrophobic alkyl tail is covalently linked to an amino acid sequence, can self-assemble into nanostructures with a broad range of applications.[5−9] Interestingly, these structures can reconfigure in response to external stimuli, including temperature, pH, and ionic strength,[10−12] which allows versatile conformations such as membrane and fiber conformations that can mimic extracellular matrixes.[13]

One interesting class of self-assembled PA molecules is based on amino acid sequences that are comprised of two domains: an amino acid sequence that gives rise to intermolecular β-sheet hydrogen bonding and a sequence of hydrophilic charged amino acids.[8,14−17] The van der Waals interactions between the tails enhance the propensity of the peptides to assemble into ordered structures, often with well-defined intermolecular hydrogen bond frameworks.[18] When the amino acids that promote β-sheet hydrogen bonding are not part of the sequence, electrostatic interactions are expected to play an even greater role in the assembly thermodynamics.

Theoretical investigations have probed the dependence of the PA assembly structures on the relative strengths of the intermolecular interactions. For example, a combined Monte Carlo, molecular dynamics (MD) simulation, and transmission electron microscopy (TEM) study on the assembly of a bioactive PA showed that when hydrogen bonding was the dominant intermolecular interaction, long (short) cylindrical micelles were formed if the electrostatic repulsion between the headgroups was weak (strong).[19,20] By contrast, under conditions where hydrogen bonding was weakened, PAs either did not assemble (strong intermolecular electrostatic repul-

Received: November 17, 2016
Revised: January 31, 2017
Published: February 1, 2017

DOI: 10.1021/acs.jpcb.6b11602
J. Phys. Chem. B 2017, 121, 1623−1628

sions) or formed spherical micelles (weak intermolecular electrostatic repulsions). This demonstrates the critical role of electrostatic interactions in the PA assembly. In general, the strength and range of these electrostatic interactions can be tuned by the solution pH and salt concentration. The pH controls the charge of the amino acids in the headgroup, and the counterions from the salt screen the intermolecular electrostatic repulsions.

Most of the experimental studies on PA assemblies have focused on the effects of the number and sequence of amino acids in the hydrogen bond forming block. Judicious choice for these parameters results in PA structures such as planar nanobelts,[21] spherical micelles,[22] helical fibers,[23] and most commonly, cylindrical nanofibers.[10,15,24]

As mentioned above, the effects of headgroup ionization have also been studied, but in systems with intermolecular hydrogen bonding interactions.[14,22,25−29] To determine purely the effects of interheadgroup electrostatic interactions, we completely eliminated the hydrogen bond forming block.

The designed molecule $C_{16}K_2$ (Figure 1a) comprises a cationic headgroup of two lysines (K), which is conjugated to a palmitoyl alkyl tail. From a broader perspective, our study deals with understanding self-assembly of amphiphiles with large ionizable headgroups. In this context, previous studies have focused on amphiphiles with small headgroups. For example, the pH-controlled micelle to vesicle transition is studied in great detail as a model for a primitive cell or protocell.[30−34] An elegant packing parameter model developed by Israelachvili[35] describes the relationship between molecular shape and morphology. Specifically, the effective molecular shape transforms from conical (charged headgroup, spherical micelle) to nearly cylindrical (uncharged headgroup, spherical vesicle). However, this model does not fully describe PA self-assembly because it does not adequately consider the steric constraints imposed by the large headgroups or other intermolecular interactions such as hydrogen bonding. Here, we investigate the structural transformations driven by charge regulation in a model system of an ionic amphiphiles with a large headgroup.

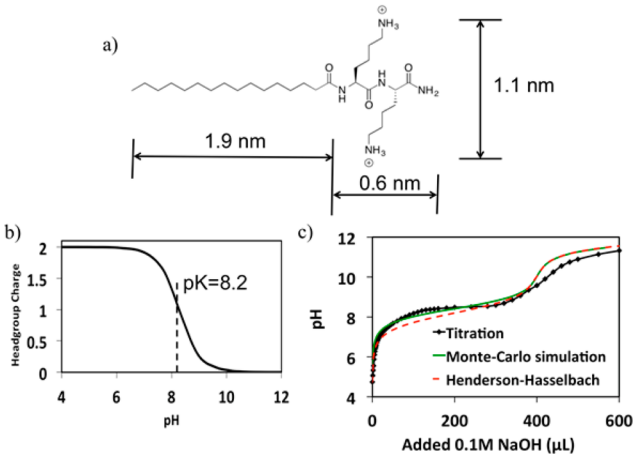

Figure 1. (a) Molecular structure of +2 charged $C_{16}K_2$ peptide with estimates for the hydrophobic tail length and hydrophilic headgroup length and width. (b) Averaged $C_{16}K_2$ headgroup charge as a function of pH in standard water environment obtained by Monte Carlo simulation, showing deprotonation around pH 8.2. (c) $C_{16}K_2$ titration curve showing how pH changes as a function of the volume of NaOH added. For comparison, calculated titration curves based on a monoprotic acid with pK = 8.2 (red, dashed) and Monte Carlo simulations (green) are shown.

RESULTS AND DISCUSSION

The synthesis of $C_{16}K_2$ with trifluoroacetate (CF_3COO^-) counterions is described in the Supporting Information (section 1.1). Figure 1b shows Monte Carlo simulations (Supporting Information, section 1.2) for the average molecular charge as a function of the solution pH. For pH < 7, the two lysine groups are fully ionized. Further increase in pH leads to a monotonic decrease in the average degree of ionization. The theoretical curve can be described by a single pK ∼ 8.2, which is substantially lower than the pK ∼ 10.0 expected for isolated lysines.[36] This implies that in $C_{16}K_2$ assemblies, the ionization tendency of lysines is reduced. This is because any arrangement of like-charged molecules in close proximity increases the overall electrostatic potential energy of the ionized state.

Figure 1c shows the measured titration curve for 4 mM $C_{16}K_2$ with 100 mM NaOH (Supporting Information, section 1.3). $C_{16}K_2$ was soluble over the entire pH range with the solutions becoming highly viscous for pH > 10. For comparison, two calculated titration curves are shown (Figure 1c). The first calculation (red, dashed) assumes that each protonated lysine is a monoprotic acid with a pK = 8.2 and uses the Henderson−Hasselbach equation (Supporting Information, section 1.2) up to the volume added of NaOH, corresponding to an equivalent concentration of PA and NaOH (equivalence point; here, 400 μL of NaOH). Thereafter, the added NaOH is assumed to only increase the solution pH. The second calculation, which reproduces the measured titration curve better up to pH ∼ 9.5 is based on the above-described Monte Carlo simulation that takes into account electrostatic correlations in the ionization process. Both of the calculations deviate from the measured titration curve in a regime where the solution became highly viscous. Nevertheless, these observations show that Monte Carlo simulations can be used to estimate a priori the ionization tendency of molecules that are in close proximity. It should be noted that the observed titration curves vary slightly between synthetic batches of $C_{16}K_2$ (see Figure S1). These differences could be due to variations in the concentration of the amphiphile or of residual salts after purification and lyophilization. Regardless, only one buffer region (plateau at pH ∼ 8) is observed in the titration curves for $C_{16}K_2$. Because morphological transformations such as the micelle to vesicle transition in fatty acids[30,37] frequently occur at pH ∼ pK, we hypothesized that a nano- or mesoscopic structural transformation would also occur at pH ∼ 8 in our system.

The structures of the $C_{16}K_2$ assembly as a function of solution pH were analyzed over micrometer to angstrom-length-scales by in situ small- and wide-angle X-ray scattering (SAXS/WAXS, Supporting Information, section 1.4) and cryo-transmission electron microscopy (cryo-TEM, Supporting Information, section 1.5). For all of the structural studies, 4 mM solutions of $C_{16}K_2$ in ultrapure water were used. The solution pH was adjusted with aqueous NaOH. Figure 2a shows the background subtracted SAXS/WAXS intensities as a function of the scattering vector magnitude $q = 4\pi\sin\theta/\lambda$. Here, λ is the X-ray wavelength, and 2θ is the scattering angle. Important changes in the intensity profiles with increasing pH can be discerned without detailed analysis (Figure 2a). First, for q < 0.3 nm^{-1}, i.e., within the SAXS regime, the I vs q slope becomes steeper for pH > 7.2. These changes in the slope are

DOI: 10.1021/acs.jpcb.6b11602
J. Phys. Chem. B 2017, 121, 1623−1628

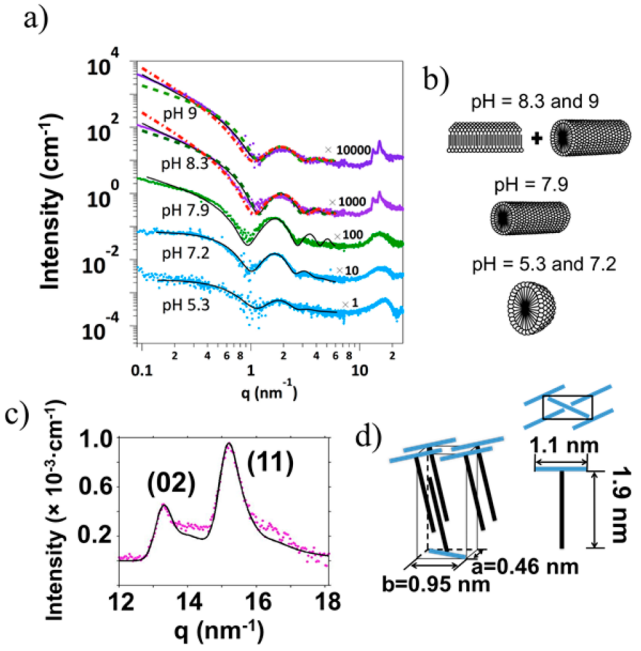

Figure 2. (a) In situ small- and wide-angle X-ray scattering data showing the background subtracted scattered intensity versus the scattering vector q for $C_{16}K_2$ as the pH is increased from 5.3 to 9. The data sets are offset vertically (×1, 10, 100, 1000, and 10 000) for clarity. The solid black curves are the best fits over the range $0.1 < q < 6$ nm^{-1} using different models. Red and green dashed curves are the separate form factors of bilayer and cylindrical micelles formed at high pH values. (b) pH-dependent self-assembly structure of $C_{16}K_2$ determined from X-ray scattering data. (c) Model fit (black curve) to background subtracted WAXS data (purple dots) for $C_{16}K_2$ at pH 9. (d) Crystalline structure of the $C_{16}K_2$ bilayer formed at pH 9 determined from WAXS fitting using a T-shape box model (bottom right figure, Supporting Information, section 2) to simulate the $C_{16}K_2$ molecule. The wide blue box approximates the headgroup, and the long black box approximates the tail. The projection of the headgroups along the bilayer normal direction shows a rectangular-P lattice (top right figure) with headgroups aligned along diagonals of the rectangle in a herringbone pattern.

related to the changes in the overall morphology of the assembly. In addition, for pH ≥ 8.3, two diffraction peaks are observed in the WAXS region ($12 < q \leq 16$ nm^{-1}), indicating the appearance of crystalline ordering in the $C_{16}K_2$ molecular packing.

First, we discuss the nanometer to micrometer scale morphological transformations that are deduced from the SAXS and cryo-TEM. Figure 2a shows the SAXS intensity profiles for pH = 5.3, 7.2, 7.9, 8.3, and 9. On the basis of the above-described Monte Carlo simulations, these pH values correspond to ∼100, 96, 75, 52, and 17% ionization of the headgroup lysines. For pH 5.3 and 7.2, when the PA headgroups are nearly fully charged, the SAXS intensity profiles (Figure 2a, bottom 2 curves) could be fitted by spherical core−shell models. For the fitting, the electron density of the core (assumed to comprise of hydrophobic tails) was constrained to be around 80% of that for pure water (ρ_w = 334 e$^-$/nm^3). This assumption is consistent with a noncrystalline, fluid-like packing of alkyl tails.[38] The most robust fitting parameters are the overall spherical radius (R_s) and the electron densities for the core (ρ_{cs}) and the shell (ρ_{ss}). For pH 5.3, R_s = 2.4 ± 0.1 nm, ρ_{cs} = 260 ± 20 e$^-$/nm^3, and ρ_{ss} = 450 ± 40 e$^-$/nm^3. For pH 7.2, R_s = 2.7 ± 0.2 nm, ρ_c = 250 ± 30 e$^-$/nm^3, and ρ_s = 450 ± 40 e$^-$/nm^3. The R_s for both pH 5.3 and 7.2 compare well with the molecular length L ∼ 2.5 nm (Figure 1a). This implies that the PA molecules assemble into spherical micelles (Figure 2b, bottom). The relatively high electron density for the spherical shell, which physically represents the PA headgroup region, suggests that the charged PA headgroups are associated with the electron-rich CF_3COO^- counterions. We note that in going from pH 5.3 to 7.2, R_s increases by ∼11%. This increase in R_s is visually detectable in SAXS intensity profiles. Specifically, the minimum at q ∼ 1 nm^{-1} shifts to a lower q value for the pH 7.2 case. However, we cannot definitively ascribe this increase to an increase in the thickness of the hydrophobic core or the hydrophilic headgroup regions because the uncertainties on these individual fitting parameters are >0.5 nm.

For pH 7.9, where ∼25% of the lysines are estimated to be uncharged, the SAXS intensity (I) profile falls off as q^{-1} in the low q region. The exponent of −1 at low q is indicative of long 1D nanostructures.[39] In fact, for q = 0.1−5 nm^{-1} range, the SAXS I vs q profile could be reasonably fitted with a cylindrical core−shell model. Similar to the spherical core−shell model, most of the SAXS profiles here can be fitted well with a radius of the cylinder R_c = 2.3 ± 0.2 nm, and the core and the shell electron densities ρ_{cs} = 275 ± 25 and ρ_{ss} = 455 ± 35 e$^-$/nm^3, respectively. The radius R_c is again close to the molecular length L. This implies that the PA assembly transforms from spherical to cylindrical micelles (Figure 2b, middle) when 30% of the lysines are expected to be uncharged. A visual confirmation of this structural phase transition was obtained via cryo-TEM. For pH 5 (spherical micelle case), only small globular aggregates were observed (Figure 3a). By contrast, for

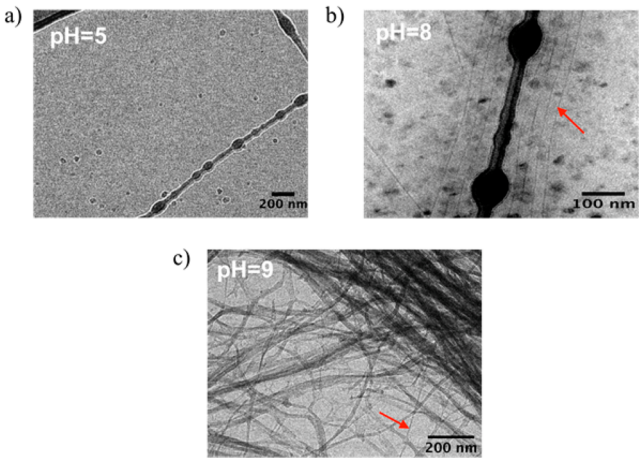

Figure 3. Representative cryogenic TEM images of self-assembly formed by $C_{16}K_2$. (a) Only spherical objects are observed at pH 5. (b) Solution at pH 8 show long fibers (red arrow). The black rod in the center is lacey carbon grid. Black stains in the background are excessive ethane from sample preparation. (c) At pH 9, flat ribbons can be observed, and there are also indications of long fibers (red arrow) similar to the fibers formed at pH 8.

pH 7.9, 1D structures with persistent lengths >100 nm (Figure 3b) were observed. Furthermore, the cryo-TEM derived nanostructure width ∼5 nm (Figure S3 in the Supporting Information) matches the SAXS-derived diameter 2 × R_c for the cylindrical micelle.

Increasing the pH to 8.3 (∼52% ionization) or 9 (∼17% ionization) results in SAXS intensities $I \propto q^{-1.4}$ and $I \propto q^{-1.5}$ in

DOI: 10.1021/acs.jpcb.6b11602
J. Phys. Chem. B 2017, 121, 1623−1628

the low q (<0.4 nm^{-1}) region, respectively. These low q exponents lie between −1 and −2, which correspond to nanostructures with extended dimensions in 1D and 2D, respectively.[39] The discussion above on 1D assembly and the amphiphilic nature of the $C_{16}K_2$ molecules suggests that at high pH, the assembly consists of mixtures of cylindrical micelles and flat bilayer membranes (Figure 2b, top). Furthermore, the increase in the magnitude of the exponent suggests that the fraction of 2D bilayers is enhanced with increasing pH. Figure 2a (top two curves) shows the fits for I vs q profiles with linear combinations of cylindrical core−shell model (dashed green lines) and a symmetric bilayer membrane model with a hydrophobic region sandwiched between two hydrophilic regions (dashed orange lines). An enlarged view of these data sets and the SAXS intensities based on the cylindrical micelle-bilayer mixture model is shown in Figure S3 (Supporting Information). This approach was verified through cryo-TEM, which showed a mixture of nanofibers and nanoribbons (Figure 3c). To reduce the free parameters in the fitting of SAXS data from the bilayer-cylindrical micelle mixture, the parameters for the cylinder component were held fixed at the best fit values obtained for pH 7.9, as described above. That is, R_c = 2.3 nm; ρ_{cs} = 275 e^-/nm^3, and ρ_{ss} = 455 e^-/nm^3. The best fit parameters for the SAXS data reveal that in going from pH 8.3 to 9, the fraction of the bilayers indeed increases from 51 ± 20 to 73 ± 20%. For the bilayer component, fitting of the SAXS data reveals thicknesses t_{tb} = 2.2 ± 0.5 nm and t_{hb} = 0.5 ± 0.1 nm for the hydrophobic tail region and each of the two headgroup regions, respectively. The hydrophobic region thickness is substantially smaller than the length of two alkyl tails. However, the enhanced electron density of the hydrophobic region $\rho_{tb} = 330^{+0}_{-60}$ e^-/nm^3 corresponds to a crystalline packing of the alkyl tails.[38] The tail crystallization is also manifested by the appearance of two diffraction peaks in the WAXS region ($12 < q \leq 16$ nm^{-1}). These observations suggest that the alkyl tails should be in their fully extended conformation with a length of 1.9 nm. Taken together, these observations imply that the two leaflets of the bilayer are strongly interdigitated. The interdigitated configuration was also recently suggested for another peptide amphiphile bilayer assembly via atomic force microscopy measurements.[21] We show via a detailed analysis of the WAXS data that the molecular packing in the interdigitated state maximizes the van der Waals interactions among the tails. It should be noted that alkyl tails of a single leaflet could not form a densely packed 2D crystalline monolayer because of the steric constraints imposed by the large headgroups. It also should be noted that both nanofibers and nanoribbons are structures with high aspect ratio. We speculate that bilayer nanoribbons formed at a high pH might evolve from cylindrical micelle nanofibers, the pathway of which is currently not well understood. Finally, the high viscosity of the solutions for pH > 10 might be a result of the formation of extended networks of nanoribbons. Overall, SAXS and cryo-TEM show that as the headgroup charge is reduced, the $C_{16}K_2$ molecular assemblies undergo transitions from spherical micelles to long cylindrical micelles to planar bilayers with the two bilayer leaflets interdigitated.

Second, we discuss the angstrom scale molecular packing within the $C_{16}K_2$ crystalline bilayers formed at pH ≥ 8.3, which is deduced from the WAXS (Figure 2c). For example, at pH 9, two diffraction peaks in the WAXS region are observed with an approximate 1:2 intensity ratio at q = 13.3 and 15.2 nm^{-1} that indicate a two-dimensional rectangular-P lattice.[40] On the basis of the multiplicity, the peak with lower intensity at q = 13.3 nm^{-1} is the (02) peak, and the peak at q = 15.2 nm^{-1} is the (11) peak. To fit the diffraction peaks, we cannot simply approximate the $C_{16}K_2$ molecule as a thin rods perpendicular to the crystalline bilayer plane because, when using this model as a repeat unit, the WAXS peak fit cannot reproduce the relative intensities and "shoulder" between these two peaks in WAXS data (Supporting Information, Figure S4). Here, we instead use a T-shaped model to simulate the $C_{16}K_2$ molecule in which the horizontal box represents the hydrophilic headgroup, and the vertical box represents the hydrophobic tail (Figure 2d, for details of the box model and WAXS analysis, see the Supporting Information, section 2). In this model, we allow the headgroup to rotate in the bilayer plane and the tail to tilt along all directions. Parameters such as thickness and electron density can be deduced from the SAXS fitting results summarized above. Following the approach detailed by Harutyunyan et al.,[41] WAXS intensity simulations powder averaged the intensities from the 2D lattices of the bilayers, which are comprised of model T-shaped $C_{16}K_2$ molecules. These simulations produced three major results. (1) The rectangular-P 2D unit cell (uc) has lattice constants a = 0.46 nm and b = 0.95 nm. (2) The basis consists of two molecules; one pointing downward at the uc origin, and one pointing upward at the uc center. The tails of both are tilted ∼33° with respect to the bilayer-normal toward the same diagonal direction of the rectangular lattice. The observed tilt reduces the intertail distance to 0.44 nm and thereby maximizes the tail−tail van der Waals' interactions.[42] (3) As shown in Figure 2d, the projection of the headgroup at the uc origin is aligned along the uc [11] diagonal direction, which is 26° from the b-axis, and the headgroup at the uc center is aligned with [−11] diagonal direction. From the top view of the bilayer lattice, the projection of the headgroups (Figure 2d) corresponds to a herringbone structure (crystallographic plane group $pgg2$). We deduce that the rotation of the headgroup results from steric constraint because the width of the headgroup (∼1.1 nm) is longer than both lattice constants (0.46 and 0.95 nm) but comparable to the diagonal length 1.06 nm. Similarly, WAXS fitting for the pH 8.3 data shows essentially the same crystalline structure with minor differences in tilt and rotation angle (Supporting Information, Figure S5). As an extension of the current study, the WAXS-predicted molecular arrangement will be refined in future grazing-incidence WAXS (GIWAXS) studies on bilayers deposited on solid substrates. This aligned geometry may also allow observation of higher order diffraction peaks, which may have been smeared out due to the intrinsic powder averaging in solution scattering, thereby yielding higher spatial resolution for molecular packing.

■ CONCLUSIONS

We designed an ionic peptide amphiphile $C_{16}K_2$ and show that charge regulation via pH can induce spherical micelles to cylindrical nanofibers to crystalline bilayer membrane structural phase transitions even in the case of amphiphilic molecules with large ionic headgroups, whereas the geometric packing parameter model suggests only spherical micelles.[35] To the best of our knowledge, the cylindrical micelle to bilayer transition has not been reported in assemblies of any PAs. This transition is concomitant with the crystallization of the amphiphilic tails. The crystalline bilayer structure shows strong interdigitation between the two leaflets and large tilts of the molecular tails. These features, which are imposed by the steric

DOI: 10.1021/acs.jpcb.6b11602
J. Phys. Chem. B 2017, 121, 1623−1628

constraints of the large ionic headgroup, are necessary for maximizing the intermolecular van der Waals' interactions. Therefore, they should be a general characteristic of the bilayer assemblies of any other molecules with headgroup dimensions much larger than the alkyl tail diameter.

■ ASSOCIATED CONTENT

Supporting Information

The Supporting Information is available free of charge on the ACS Publications website at DOI: 10.1021/acs.jpcb.6b11602.

Detailed experimental and simulation methods and supplementary figures (PDF)

■ AUTHOR INFORMATION

Corresponding Authors

*E-mail: m-olvera@northwestern.edu.
*E-mail: bedzyk@northwestern.edu.

ORCID

Samuel I. Stupp: 0000-0002-5491-7442
Michael J. Bedzyk: 0000-0002-1026-4558

Notes

The authors declare no competing financial interest.

■ ACKNOWLEDGMENTS

This research was primarily supported by the Department of Energy (DOE), Office of Basic Energy Sciences under Contract DE-FG02-08ER46539. Additional support to L.C.P and S.I.S. for peptide synthesis was provided by the National Science Foundation (Grant DMR-1006713). Peptide synthesis was performed in the Peptide Synthesis Core Facility of the Simpson Querrey Institute at Northwestern University. The U.S. Army Research Office, the U.S. Army Medical Research and Materiel Command, and Northwestern University provided funding to develop this facility. The SAXS/WAXS experiments were performed at the DuPont-Northwestern-Dow Collaborative Access Team (DND-CAT) located at Sector 5 of the Advanced Photon Source (APS) and at APS Sector 12. DND-CAT is supported by E.I. DuPont de Nemours & Co., The Dow Chemical Company, and Northwestern University. The APS, an Office of Science User Facility operated for the DOE by Argonne National Laboratory, is supported by the DOE under Contract DE-AC02-06CH11357. TEM was done in the EPIC facility at Northwestern University and was supported by the Soft and Hybrid Nanotechnology Experimental (SHyNE) (Grant NSF NNCI-1542205), the MRSEC (Grant NSF DMR-1121262), and the International Institute for Nanotechnology (IIN). The authors thank M. Karver for assistance with the peptide synthesis and S. Weigand (DND-CAT) and B. Lee (APS, sector 12) for assistance with the X-ray scattering measurements.

■ REFERENCES

(1) Qiao, B. F.; Ferru, G.; Olvera de la Cruz, M.; Ellis, R. J. Molecular Origins of Mesoscale Ordering in a Metalloamphiphile Phase. *ACS Cent. Sci.* **2015**, *1*, 493−503.

(2) Qiao, B.; Demars, T.; Olvera de la Cruz, M.; Ellis, R. J. How Hydrogen Bonds Affect the Growth of Reverse Micelles around Coordinating Metal Ions. *J. Phys. Chem. Lett.* **2014**, *5*, 1440−1444.

(3) Dourdain, S.; Hofmeister, I.; Pecheur, O.; Dufreche, J. F.; Turgis, R.; Leydier, A.; Jestin, J.; Testard, F.; Pellet-Rostaing, S.; Zemb, T. Synergism by Coassembly at the Origin of Ion Selectivity in Liquid-Liquid Extraction. *Langmuir* **2012**, *28*, 11319−11328.

(4) Arnold, M. S.; Guler, M. O.; Hersam, M. C.; Stupp, S. I. Encapsulation of Carbon Nanotubes by Self-assembling Peptide Amphiphiles. *Langmuir* **2005**, *21*, 4705−4709.

(5) Cui, H. G.; Webber, M. J.; Stupp, S. I. Self-Assembly of Peptide Amphiphiles: From Molecules to Nanostructures to Biomaterials. *Biopolymers* **2010**, *94*, 1−18.

(6) Versluis, F.; Marsden, H. R.; Kros, A. Power Struggles in Peptide-amphiphile Nanostructures. *Chem. Soc. Rev.* **2010**, *39*, 3434−3444.

(7) Hamley, I. W. Self-assembly of Amphiphilic Peptides. *Soft Matter* **2011**, *7*, 4122−4138.

(8) Dehsorkhi, A.; Castelletto, V.; Hamley, I. W. Self-assembling Amphiphilic Peptides. *J. Pept. Sci.* **2014**, *20*, 453−467.

(9) Matson, J. B.; Zha, R. H.; Stupp, S. I. Peptide Self-assembly for Crafting Functional Biological Materials. *Curr. Opin. Solid State Mater. Sci.* **2011**, *15*, 225−235.

(10) Zhang, S. M.; Greenfield, M. A.; Mata, A.; Palmer, L. C.; Bitton, R.; Mantei, J. R.; Aparicio, C.; Olvera de la Cruz, M.; Stupp, S. I. A Self-assembly Pathway to Aligned Monodomain Gels. *Nat. Mater.* **2010**, *9*, 594−601.

(11) Tantakitti, F.; Boekhoven, J.; Wang, X.; Kazantsev, R. V.; Yu, T.; Li, J. H.; Zhuang, E.; Zandi, R.; Ortony, J. H.; Newcomb, C.; Stupp, S. I.; et al. Energy Landscapes and Functions of Supramolecular Systems. *Nat. Mater.* **2016**, *15*, 469−476.

(12) Miravet, J. F.; Escuder, B.; Segarra-Maset, M. D.; Tena-Solsona, M.; Hamley, I. W.; Dehsorkhi, A.; Castelletto, V. Self-assembly of a Peptide Amphiphile: Transition from Nanotape Fibrils to Micelles. *Soft Matter* **2013**, *9*, 3558−3564.

(13) Beniash, E.; Hartgerink, J. D.; Storrie, H.; Stendahl, J. C.; Stupp, S. I. Self-assembling Peptide Amphiphile Nanofiber Matrices for Cell Entrapment. *Acta Biomater.* **2005**, *1*, 387−397.

(14) Chen, Y. R.; Gan, H. X.; Tong, Y. W. pH-Controlled Hierarchical Self-Assembly of Peptide Amphiphile. *Macromolecules* **2015**, *48*, 2647−2653.

(15) Hartgerink, J. D.; Beniash, E.; Stupp, S. I. Self-assembly and Mineralization of Peptide-amphiphile Nanofibers. *Science* **2001**, *294*, 1684−1688.

(16) Ortony, J. H.; Newcomb, C. J.; Matson, J. B.; Palmer, L. C.; Doan, P. E.; Hoffman, B. M.; Stupp, S. I. Internal Dynamics of a Supramolecular Nanofibre. *Nat. Mater.* **2014**, *13*, 812−816.

(17) Lowik, D. W. P. M.; van Hest, J. C. M. Peptide Based Amphiphiles. *Chem. Soc. Rev.* **2004**, *33*, 234−245.

(18) Aggeli, A.; Bell, M.; Boden, N.; Keen, J. N.; McLeish, T. C. B.; Nyrkova, I.; Radford, S. E.; Semenov, A. Engineering of Peptide Beta-sheet Nanotapes. *J. Mater. Chem.* **1997**, *7*, 1135−1145.

(19) Velichko, Y. S.; Stupp, S. I.; Olvera de la Cruz, M. Molecular Simulation Study of Peptide Amphiphile Self-assembly. *J. Phys. Chem. B* **2008**, *112*, 2326−2334.

(20) Tsonchev, S.; Niece, K. L.; Schatz, G. C.; Ratner, M. A.; Stupp, S. I. Phase diagram for Assembly of Biologically-active Peptide Amphiphiles. *J. Phys. Chem. B* **2008**, *112* (2), 441−447.

(21) Cui, H.; Muraoka, T.; Cheetham, A. G.; Stupp, S. I. Self-Assembly of Giant Peptide Nanobelts. *Nano Lett.* **2009**, *9*, 945−951.

(22) Ghosh, A.; Haverick, M.; Stump, K.; Yang, X. Y.; Tweedle, M. F.; Goldberger, J. E. Fine-Tuning the pH Trigger of Self-Assembly. *J. Am. Chem. Soc.* **2012**, *134*, 3647−3650.

(23) Aggeli, A.; Nyrkova, I. A.; Bell, M.; Harding, R.; Carrick, L.; McLeish, T. C. B.; Semenov, A. N.; Boden, N. Hierarchical Self-assembly of Chiral Rod-like Molecules as a Model for Peptide Beta-sheet Tapes, Ribbons, Fibrils, and Fibers. *Proc. Natl. Acad. Sci. U. S. A.* **2001**, *98* (21), 11857−11862.

(24) Hartgerink, J. D.; Beniash, E.; Stupp, S. I. Peptide-amphiphile nanofibers: A Versatile Scaffold for the Preparation of Self-assembling Materials. *Proc. Natl. Acad. Sci. U. S. A.* **2002**, *99*, 5133−5138.

(25) Jin, Y.; Xu, X. D.; Chen, C. S.; Cheng, S. X.; Zhang, X. Z.; Zhuo, R. X. Bioactive Amphiphilic Peptide Derivatives with pH Triggered Morphology and Structure. *Macromol. Rapid Commun.* **2008**, *29*, 1726−1731.

DOI: 10.1021/acs.jpcb.6b11602
J. Phys. Chem. B 2017, 121, 1623−1628

(26) Liang, J.; Wu, W. L.; Xu, X. D.; Zhuo, R. X.; Zhang, X. Z. pH Responsive Micelle Self-assembled from a new Amphiphilic Peptide as Anti-tumor Drug Carrier. *Colloids Surf., B* **2014**, *114*, 398−403.
(27) Dehsorkhi, A.; Castelletto, V.; Hamley, I. W.; Adamcik, J.; Mezzenga, R. The Effect of pH on the Self-assembly of a Collagen Derived Peptide Amphiphile. *Soft Matter* **2013**, *9*, 6033−6036.
(28) Moyer, T. J.; Finbloom, J. A.; Chen, F.; Toft, D. J.; Cryns, V. L.; Stupp, S. I. pH and Amphiphilic Structure Direct Supramolecular Behavior in Biofunctional Assemblies. *J. Am. Chem. Soc.* **2014**, *136*, 14746−14752.
(29) Webber, M. J.; Newcomb, C. J.; Bitton, R.; Stupp, S. I. Switching of Self-assembly in a Peptide Nanostructure with a Specific Enzyme. *Soft Matter* **2011**, *7*, 9665−9672.
(30) Monnard, P. A.; Deamer, D. W. Membrane Self-assembly Processes: Steps toward the First Cellular Life. *Anat. Rec.* **2002**, *268*, 196−207.
(31) Egelhaaf, S. U.; Schurtenberger, P. Micelle-to-vesicle Transition: A Time-resolved Structural Study. *Phys. Rev. Lett.* **1999**, *82*, 2804−2807.
(32) Yang, Y.; Dong, J. F.; Li, X. F. Micelle to Vesicle Transitions of N-dodecyl-1, omega-diaminoalkanes: Effects of pH, Temperature and Salt. *J. Colloid Interface Sci.* **2012**, *380*, 83−89.
(33) Wang, W.; Lu, W.; Jiang, L. Influence of pH on the Aggregation Morphology of a Novel Surfactant with Single Hydrocarbon Chain and Multi-amine Headgroups. *J. Phys. Chem. B* **2008**, *112*, 1409−1413.
(34) Lu, H. S.; Wang, L.; Huang, Z. Y. Unusual pH-responsive Fluid Based on a Simple Tertiary Amine Surfactant: the Formation of Vesicles and Wormlike Micelles. *RSC Adv.* **2014**, *4*, 51519−51527.
(35) Israelachvili, J. N. *Intermolecular and Surface Forces*, 3rd ed.; Elsevier, Inc.: Amsterdam, Netherlands, 2011.
(36) Leung, C. Y.; Palmer, L. C.; Kewalramani, S.; Qiao, B. F.; Stupp, S. I.; Olvera de la Cruz, M.; Bedzyk, M. J. Crystalline Polymorphism Induced by Charge Regulation in Ionic Membranes. *Proc. Natl. Acad. Sci. U. S. A.* **2013**, *110*, 16309−16314.
(37) Dzieciol, A. J.; Mann, S. Designs for life: Protocell Models in the Laboratory. *Chem. Soc. Rev.* **2012**, *41*, 79−85.
(38) Fukuto, M.; Heilmann, R. K.; Pershan, P. S.; Yu, S. J. M.; Soto, C. M.; Tirrell, D. A. Internal Segregation and Side Chain Ordering in Hairy-rod Polypeptide Monolayers at the Gas/Water Interface: An X-ray Scattering Study. *J. Chem. Phys.* **2003**, *119*, 6253−6270.
(39) Jens Als-Nielsen, D. M. *Elements of Modern X-ray Physics*, 2nd ed.; Wiley: Hoboken, NJ, 2011.
(40) Leung, C. Y.; Palmer, L. C.; Qiao, B. F.; Kewalramani, S.; Sknepnek, R.; Newcomb, C. J.; Greenfield, M. A.; Vernizzi, G.; Stupp, S. I.; Bedzyk, M. J.; Olvera de la Cruz, M. Molecular Crystallization Controlled by pH Regulates Mesoscopic Membrane Morphology. *ACS Nano* **2012**, *6*, 10901−10909.
(41) Harutyunyan, B.; Dannenhoffer, A.; Kewalramani, S.; Aytun, T.; Fairfield, D. J.; Stupp, S. I.; Bedzyk, M. J. Molecular Packing of Amphiphilic Nanosheets Resolved by X-ray Scattering. *J. Phys. Chem. C* **2017**, *121*, 1047−1054.
(42) Kaganer, V. M.; Mohwald, H.; Dutta, P. Structure and Phase Transitions in Langmuir Monolayers. *Rev. Mod. Phys.* **1999**, *71*, 779−819.

DOI: 10.1021/acs.jpcb.6b11602
J. Phys. Chem. B 2017, 121, 1623−1628